

THE PANCHROMATIC HUBBLE ANDROMEDA TREASURY. XXX. SYNTHETIC ULTRAVIOLET FLUX MAPS OF M31 FROM RESOLVED OPTICAL PHOTOMETRY.*

JACOB E. SIMONES¹, ALEXIA R. LEWIS², BENJAMIN D. JOHNSON⁴, JULIANNE J. DALCANTON², ANDREW E. DOLPHIN³, EVAN D. SKILLMAN¹, DANIEL R. WEISZ^{4,5}, BENJAMIN F. WILLIAMS²

Draft version March 11, 2015

ABSTRACT

Starting from star formation histories based on color magnitude diagrams, we have used stellar population synthesis to create maps of synthetic far- and near-ultraviolet (FUV and NUV) flux at sub-kpc resolution for the northeast quadrant of M31. The synthetic maps reproduced all of the main morphological features found in corresponding maps of observed FUV and NUV flux, including rings and large star-forming complexes. Comparing the flux maps pixel-by-pixel, we found the median synthetic-to-observed flux ratios to be $1.02 +0.74/-0.43$ in FUV and $0.79 +0.35/-0.24$ in NUV. The synthetic fluxes were therefore consistent overall with the observed fluxes in both filters. We used the observed fluxes and standard flux calibrations to derive star formation rate (SFR) maps, which we compared with a map of the mean SFRs over the last 100 Myr of the star formation histories (SFHs). We determined a lower limit of $\text{SFR} \sim 10^{-5} M_{\odot} \text{ yr}^{-1}$ below which the commonly assumed linear relationship between UV flux and SFR appears to break down. Above this limit, we found the median ratios of the flux-based SFRs to the mean SFRs to be $0.57 +0.47/-0.26$ in FUV and $1.24 +0.88/-0.52$ in NUV. Both the FUV and NUV flux-based SFRs were therefore consistent overall with the mean SFRs derived from the SFHs. Integrating over the entire mean SFR map, we found a global SFR of $0.3 M_{\odot} \text{ yr}^{-1}$. The corresponding measurements from the flux-based SFR maps were factors of 0.74 (FUV) and 1.45 (NUV) of the global mean SFR value. It is not yet understood why the SFR ratios in the global case are larger than the median pixel-wise ratios. The primary source of uncertainty in both the synthetic flux maps and the flux-based SFR maps was most likely incomplete IMF sampling due to the small pixel areas. With the exception of the faintest areas of the galaxy, we did not identify any trends for flux or SFR with environment.

Keywords: galaxies: evolution – galaxies: individual (M31) – galaxies: photometry – galaxies: star formation – galaxies: stellar content

1. INTRODUCTION

M31 is a well-studied, large spiral galaxy and has been observed at a variety of wavelengths, e.g., in the ultraviolet (UV) by the *Galaxy Evolution Explorer* (*GALEX*; Morrissey et al. 2007), in the optical, including H α , for the Local Group Galaxies Survey (Massey et al. 2006), and in the infrared by the *Spitzer Space Telescope* (Gordon et al. 2006). The wealth of high-quality data available for M31 provides a valuable opportunity to model various observations and test our current understanding of stellar astrophysics. In particular, the initial mass function (IMF), models of stellar evolution and stellar spectra, and extinction curves are all required to model the integrated light from galaxies.

A critical ingredient for modeling the flux from a galaxy is a detailed knowledge of its star formation history (SFH). Deriving SFHs by color-magnitude diagram (CMD) analysis is a reliable method that can be used whenever photometry of resolved stars is available. An extensive optical photometric catalog for M31 has been compiled by the Panchromatic Hubble Andromeda Treasury (PHAT; Dalcanton et al. 2012; Williams et al. 2014), and Lewis et al. (2015) have used these data to derive the spatially resolved SFH of the northeast quadrant. With sub-kpc resolution, this SFH dataset is the ideal input for stellar population synthesis codes that model total flux given a population’s star formation rate (SFR) and metallicity evolution. The result is a set of spatially resolved maps of synthetic broadband flux in M31 which can be compared with observations.

* Based on observations made with the NASA/ESA *Hubble Space Telescope*, obtained from the Data Archive at the Space Telescope Science Institute, which is operated by the Association of Universities for Research in Astronomy, Inc., under NASA contract NAS 5-26555.

¹ Minnesota Institute for Astrophysics, University of Minnesota, 116 Church Street SE, Minneapolis, MN 55455, USA; jsimones@astro.umn.edu; skillman@astro.umn.edu

² Department of Astronomy, Box 351580, University of Washington, Seattle, WA 98195, USA; jd@astro.washington.edu; ben@astro.washington.edu

³ Raytheon, 1151 E. Hermans Road, Tucson, AZ 85756, USA; adolphin@raytheon.com

⁴ Department of Astronomy, University of California at Santa Cruz, 1156 High Street, Santa Cruz, CA 95064, USA; drw@ucsc.edu, bjohnso6@ucsc.edu

⁵ Hubble Fellow

The Lewis et al. (2015) SFHs can also be used to create temporally averaged SFR maps. Because the SFHs were derived from the resolved stars without any prior assumptions about the SFHs, such maps provide a standard against which flux-based SFR estimates (e.g., using any of the calibrations from Kennicutt & Evans 2012) can be tested. Using integrated flux to estimate SFRs for distant galaxies, where resolved stars are not available, is a common technique in extragalactic astronomy. Previous studies have investigated how flux-based SFR estimators hold up against resolved-star SFHs in sub-kpc UV-bright regions (Simones et al. 2014) and in low-metallicity dwarf galaxies (Johnson et al. 2013; McQuinn

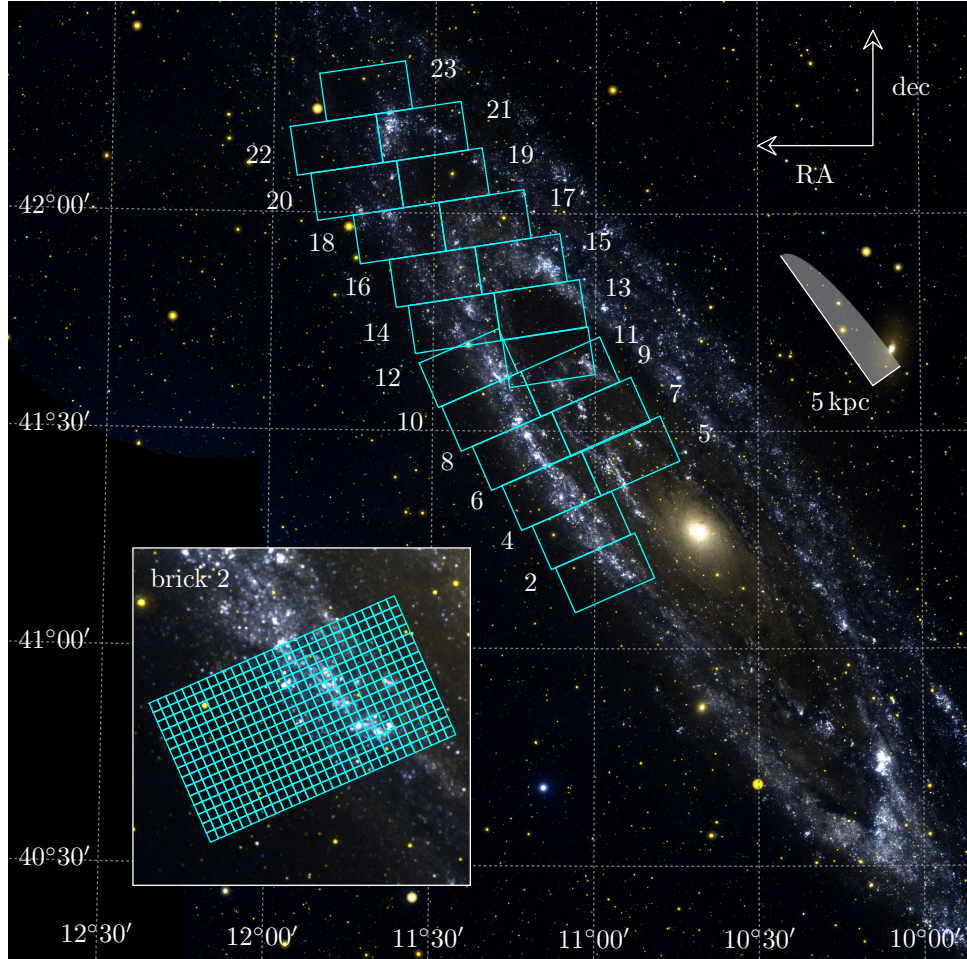


Figure 1. Map of the PHAT survey area. The 21 PHAT bricks analyzed in this study are outlined and numbered. Each brick was divided into 450 regions on a 15×30 grid, as shown for brick 2 in the inset panel. Lewis et al. (2015) derived the SFHs for all of the ~ 24 arcsec \times 27 arcsec regions.

et al. 2015). The SFHs of Lewis et al. (2015) based on data from PHAT make it possible to broaden this type of analysis to include a wide variety of environments in a large local group spiral galaxy.

In this study, we have used the PHAT CMD-based SFHs and stellar population synthesis to create maps of synthetic UV flux at sub-kpc resolution for the northeast quadrant of M31. We then compared the synthetic flux maps with observations from *GALEX*. We have focused only on *GALEX* FUV and NUV (far and near UV), though this work can be extended to other wavelength regimes. In §2, we describe the SFH dataset and the production of the synthetic flux maps. §3 describes the process of producing observed flux maps from *GALEX* FUV and NUV images. The creation of SFR maps both from the SFHs and the observed fluxes using common flux-SFR calibrations are described in §4. In §5, we compare the synthetic maps with the observations and compare mean SFR maps with SFRs estimated from observed flux. We conclude in §6.

2. SYNTHETIC UV FLUX MAPS

2.1. The spatially resolved star formation history of M31

The PHAT survey (Dalcanton et al. 2012; Williams et al. 2014) measured multiband photometry for over

117 million resolved stars in M31 using the *Hubble Space Telescope* (*HST*). The PHAT survey area is shown in Figure 1. Lewis et al. (2015) used photometry in the two optical bands (F475W and F814W, observed with the Advanced Camera for Surveys, ACS, instrument) to derive spatially resolved SFHs for the northeast quadrant of M31, excluding the crowded bulge area. To summarize their work, each brick (using PHAT terminology; see Figure 1) in the PHAT survey (except bricks 1 and 3) was divided into 450 regions on a uniform 15×30 grid, with each region ~ 24 arcsec \times 27 arcsec in size. The F475W, F814W CMD of each region was then fit using the CMD modeling code MATCH (Dolphin 2002) to determine the most likely SFH under the following assumptions:

1. The Kroupa (2001) IMF.
2. The Padova isochrones (Marigo et al. 2008) with updated asymptotic giant branch tracks (Girardi et al. 2010).
3. A binary fraction of 0.35 with a uniform mass ratio.
4. A distance modulus of 24.47 (McConnachie et al. 2005).

5. Age resolutions of 0.1 dex for $6.60 \leq \log_{10}(\text{age}) \leq 9.90$ and 0.25 dex for $9.90 < \log_{10}(\text{age}) \leq 10.15$.
6. A metallicity resolution of 0.1 dex over the range $-2.3 \leq [\text{M}/\text{H}] \leq 0.1$, constrained to increase monotonically over time.
7. A two-parameter extinction model consisting of a total foreground component, A_{Vf} , and an additional differential component following a uniform distribution from 0 to a maximum value, dA_V . The A_{Vf} and dA_V parameters were optimized for each region (see also Simones et al. 2014).

In addition, the portion of each CMD with $\text{F475W} - \text{F814W} > 1.25$ and $\text{F475W} > 21$ (red giant branch and red clump stars) was excluded from the fit. This was done to ensure that the optimized extinction parameters corresponded only to the dust associated with the young, UV-producing stars on the main sequence.

2.2. Broadband UV flux modeling

We used the SFHs (§2.1) to model broadband UV fluxes, allowing us to create synthetic UV flux maps for the PHAT survey area. Past studies have used CMD-based SFHs to model fluxes, including Gogarten et al. (2009) for UV-bright regions in the outer disk of M81, Johnson et al. (2013) for dwarf galaxies in the Local Volume, and more recently Simones et al. (2014) for a small sample of UV-bright regions in M31. Our work builds directly on the analysis of Simones et al. (2014) by extending our coverage to the entire PHAT survey area to include a wide variety of environments. We focused on modeling fluxes in the *GALEX* FUV and NUV filters only. However, because we begin by modeling spectral energy distributions (SEDs), the process we describe below can be generalized to model fluxes in any set of filters assuming the range of ages covered by the SFHs is sufficient.

The flux in a given region was modeled using a technique based on that described in Johnson et al. (2013). We began with a set of simple stellar population (SSP) models generated using the Flexible Stellar Population Synthesis (FSPS) code (Conroy et al. 2009; Conroy & Gunn 2010). For consistency with Lewis et al. (2015), we ran FSPS assuming the Kroupa (2001) IMF and the Padova isochrones (Marigo et al. 2008) with updated asymptotic giant branch tracks (Girardi et al. 2010). We also chose the BaSeL 3.1 semi-empirical stellar SED library (Westera et al. 2002). The SSPs were aged from $\log(\text{age}) = 5.500$ to 10.175 in steps of 0.025 dex. We set the SSP metallicities independently for each region using the mean metallicity over the last 100 Myr of the SFH (the 100 Myr timescale corresponds to the lifetime of UV emission). If the SFR was consistently zero over the last 100 Myr, then we instead set the metallicity to the most recent metallicity where $\text{SFR} > 0$.

We applied the SSP models to a region’s SFH to model its integrated SED. We first processed the SFH by rescaling the youngest age bin to include all ages up to the present (the Padova isochrones are only available for $\log_{10}(\text{age}) \geq 6.60$), and increasing the age resolution of the full SFH to 20 samples per age bin. The subsampled SFH was then interpolated to the series of ages in the set

Table 1
GALEX filter properties.

	FUV	NUV
Unit response, U_X ($\times 10^{-15} \text{ erg s}^{-1} \text{ cm}^{-2} \text{ \AA}^{-1}$) ^a	1.40	0.206
AB magnitude zeropoint, Z_X ^a	18.82	20.08
Effective wavelength (\AA) ^b	1538.6	2315.7

^a http://galex1.gsfc.nasa.gov/docs/galex/FAQ/counts_background.html

^b Morrissey et al. (2007)

of SSP models. The SED of each SSP was weighted by the mass of its corresponding age bin from the SFH, and the individual SSP SEDs were finally summed to derive the integrated intrinsic (i.e., unattenuated) model SED.

We derived an attenuated SED for the region using the same two-component extinction model used by MATCH to fit the CMD together with the region’s best-fit A_{Vf} and dA_V parameters (Lewis et al. 2015). To do this, we divided the intrinsic SED into 30 identical component SEDs (larger numbers of components did not significantly improve the accuracy of our results). Each component was attenuated according to the Cardelli et al. (1989) extinction curve with a uniform random A_V drawn between A_{Vf} and $A_{Vf} + dA_V$. The Cardelli et al. (1989) extinction curve predicts the amount of extinction relative to that in the V band, A_V , as a function of wavelength and is based on the average extinction in the Galaxy with a total-to-selective extinction ratio of $R_V = 3.1$. Previous studies have shown that this extinction curve is applicable to M31 as a whole in both the UV (Bianchi et al. 1996) and the optical (Barmby et al. 2000) regimes. Finally, the attenuated SED components were summed to obtain the region’s integrated attenuated model SED.

The intrinsic and the attenuated model SEDs were weighted by the response curves for the *GALEX* FUV and NUV filters to obtain absolute synthetic FUV and NUV magnitudes in the AB system. The absolute magnitudes were converted into apparent magnitudes for the region by assuming a distance modulus of 24.47 (McConnachie et al. 2005).

Using a subscript (indicated here by X) to refer to either FUV or NUV, the conversion between absolute magnitude, m_X , and flux, f_X , in filter X is given by,

$$m_X = -2.5 \log_{10} \left(\frac{f_X}{U_X} \right) + Z_X , \quad (1)$$

where the *GALEX* unit responses, U_X , and zeropoints, Z_X , are given in Table 1. We used the apparent magnitudes and Equation 1 to derive the intrinsic and the attenuated broadband UV fluxes for the region, denoted by $f_X^{\text{SFH},0}$ and f_X^{SFH} , respectively.

After modeling the intrinsic and attenuated fluxes for all of the regions in a brick, we assembled the flux values (for a given filter) into a 15×30 array to form an image mapping the synthetic flux across the brick. The brick map was independently tied to a world coordinate system using a 2D least-squares optimization to find the best-fit CD matrix (Calabretta & Greisen 2002) for a gnomonic

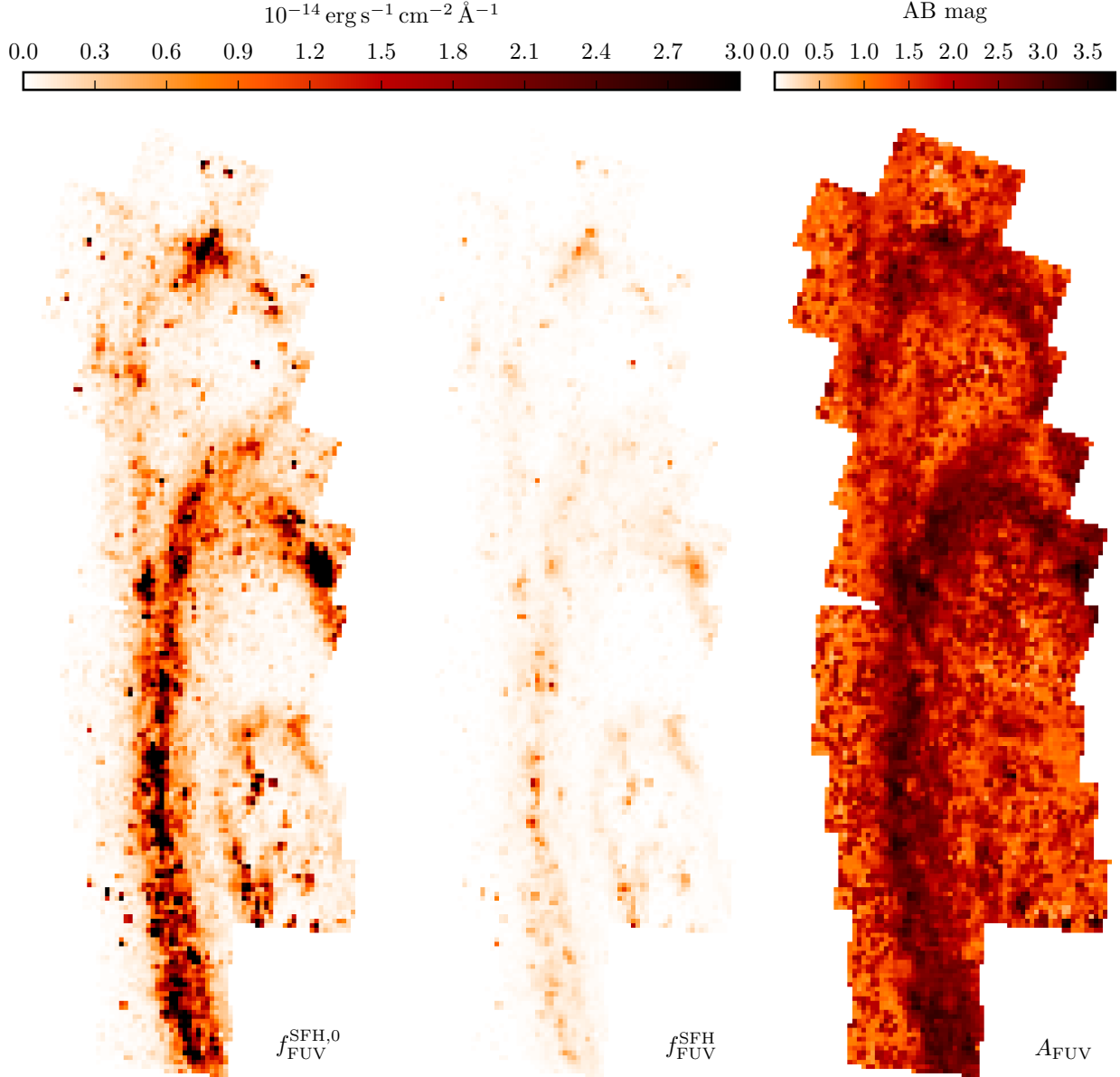


Figure 2. FUV flux modeled from the SFHs. The intrinsic flux, $f_{\text{FUV}}^{\text{SFH},0}$, is shown in the left panel and the middle panel shows the flux attenuated according to the extinction model, $f_{\text{FUV}}^{\text{SFH}}$ (also shown alongside the observed GALEX FUV flux in Figure 4). The FUV extinction, A_{FUV} , derived from $f_{\text{FUV}}^{\text{SFH},0}$ and $f_{\text{FUV}}^{\text{SFH}}$ is shown on the right.

tangent plane projection using the known RA and DEC coordinates of the brick grid vertices measured by Lewis et al. (2015). We repeated this process for all of the bricks, resulting in a set of 21 brick maps. We then reprojected and added the brick maps using Montage⁷ to create full maps, or mosaics, of synthetic FUV and NUV flux for the PHAT survey area.

All of the mosaic maps are registered to a grid defined by a template header that was automatically chosen by Montage as the best fit to the collection of input brick maps. The mosaic grid has a pixel scale of 23.75 arcsec,

which is comparable to the sizes of the regions from the original brick grids defined in Lewis et al. (2015). Assuming a distance modulus of 24.47 (McConnachie et al. 2005), a disk inclination of 78 deg (Tully 1994), and a major axis position angle of 35 deg (de Vaucouleurs et al. 1995), the pixel scale is deprojected to a linear size of $dx = 440 \text{ pc}$ and $dy = 100 \text{ pc}$ approximately along the minor and major axes of M31, respectively. The synthetic flux maps therefore have a resolution that is firmly in the sub-kpc regime.

The final synthetic flux maps, $f_X^{\text{SFH},0}$ and f_X^{SFH} , are

⁷ <http://montage.ipac.caltech.edu/>

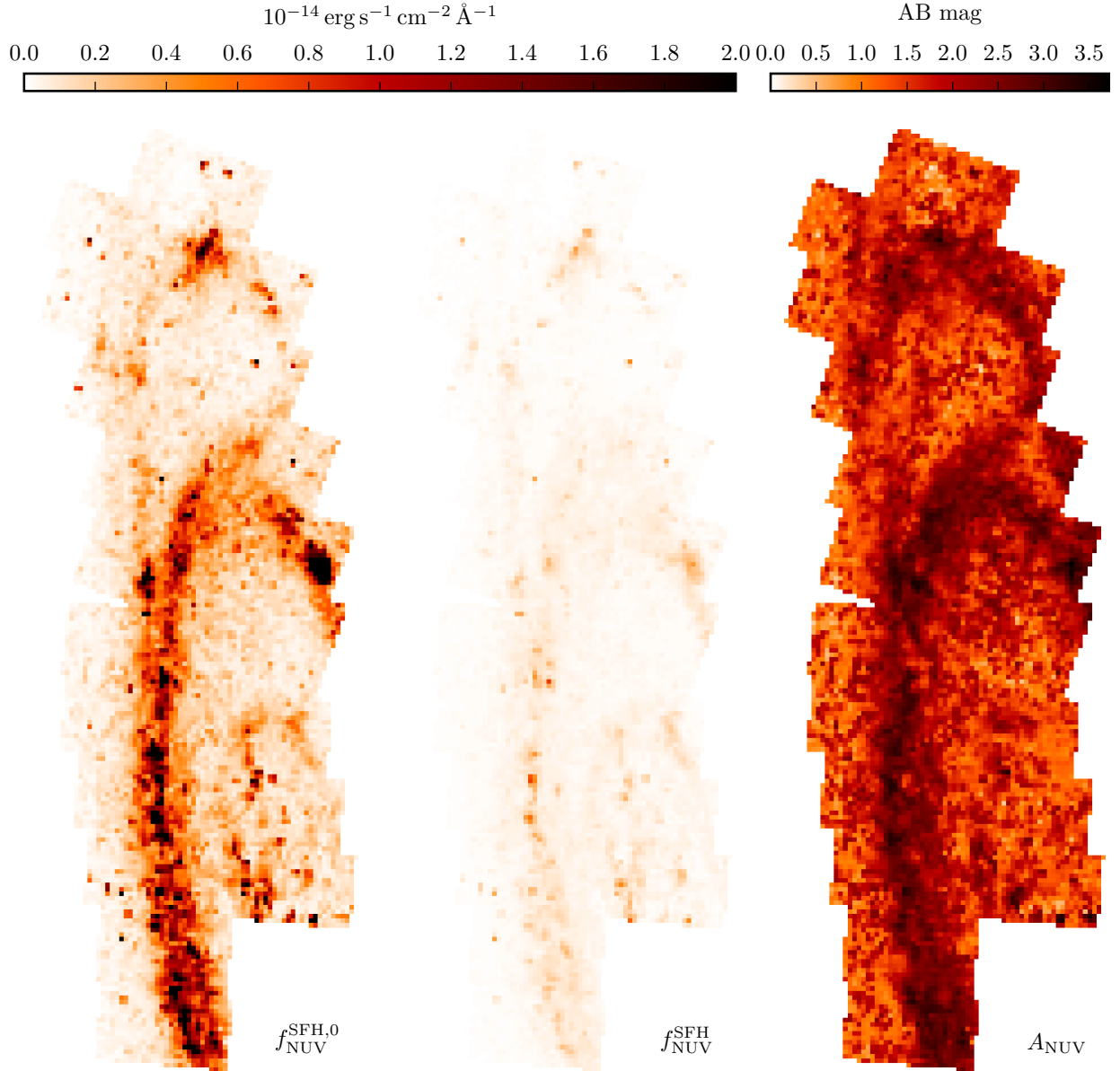


Figure 3. Same as Figure 2, but for the NUV filter.

shown in Figures 2 (FUV) and 3 (NUV).⁸

We used the synthetic flux maps to derive maps of A_X^{SFH} , the total extinctions in the FUV and NUV bands. The intrinsic and attenuated flux maps were converted into AB magnitudes, $m_X^{\text{SFH},0}$ and m_X^{SFH} , using Equation 1. The extinction maps were then calculated as the difference between the attenuated and the intrinsic magnitudes, $A_X^{\text{SFH}} = m_X^{\text{SFH}} - m_X^{\text{SFH},0}$. We show the synthetic extinction maps with their corresponding synthetic flux maps in Figures 2 and 3.

A pixel weight map representing the coverage of the

⁸ The synthetic and the observed flux maps, as well as the 100 Myr mean SFR map, are available at <https://github.com/jesaerys/m31flux>.

available PHAT data was also produced during the mosaicking process. Mosaic pixels fully within the PHAT survey border (excluding bricks 1 and 2 near the bulge) have a weight of 1, pixels fully outside the border have a weight of 0, and all other pixels have weights between 0 and 1 depending on the fraction of the pixel area within the survey border. Throughout this study we used the weight map to mask out all pixels not fully within the survey border so that our comparisons with observations are done on a full-pixel basis.

3. GALEX OBSERVATIONS

We constructed maps of observed *GALEX* FUV and NUV flux, f_X^{obs} , to match the synthetic flux maps described in §2.2. We started with the intensity maps of

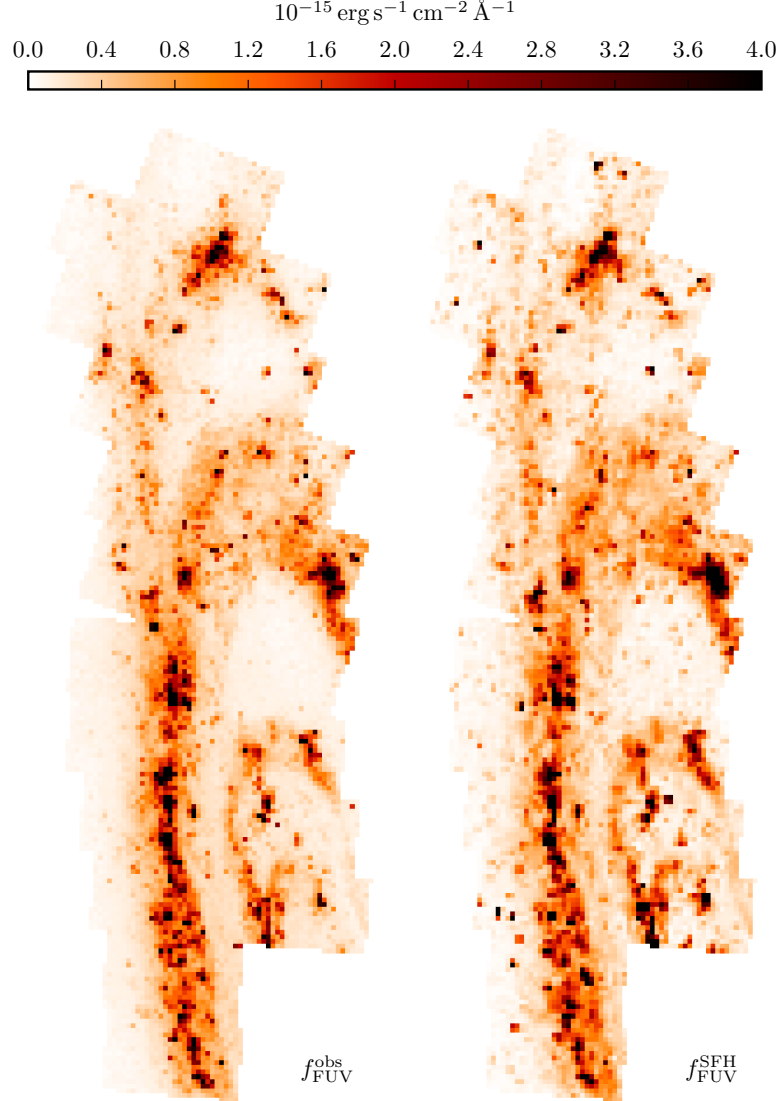


Figure 4. Observed FUV flux from GALEX, $f_{\text{FUV}}^{\text{obs}}$ (left), and synthetic attenuated FUV flux from the SFHs, $f_{\text{FUV}}^{\text{SFH}}$ (right). The observed map has been clipped to the PHAT survey border to match the synthetic map. The synthetic fluxes show excellent morphological agreement with the observed fluxes.

Table 2
GALEX observations.

Filter	Tile name
FUV	PS_M31_MOS00-fd-int.fits
	PS_M31_MOS07-fd-int.fits
	PS_M31_MOS08-fd-int.fits
	PS_M31_MOS09-fd-int.fits
	PS_M31_MOS10-fd-int.fits
NUV	PS_M31_MOS00-nd-int.fits
	PS_M31_MOS07-nd-int.fits
	PS_M31_MOS08-nd-int.fits
	PS_M31_MOS09-nd-int.fits
	PS_M31_MOS10-nd-int.fits

five tiles in the *GALEX* Deep Imaging Survey (DIS; Martin et al. 2005) covering the PHAT survey area (see Table 2). The tiles were converted from count rate units, cps,

into flux according to,

$$f_X = U_X \left(\frac{\text{cps}_X}{\text{counts s}^{-1} \text{ pixel}^{-1}} \right), \quad (2)$$

where U_X is given in Table 1. We then used Montage to reproject the flux tiles to the same template header as the synthetic flux mosaics (see §2), match the background levels of the tiles, and add the tiles together to create the final mosaic.

A small amount of background UV flux was present in the FUV and NUV mosaics, primarily due to scattering of UV photons from hot foreground stars in the Galaxy. We measured the mean background flux in a rectangular aperture in an off-galaxy area relatively devoid of stars in the reprojected, background-matched tile PS_M31_MOS07. The resulting FUV and NUV background levels were

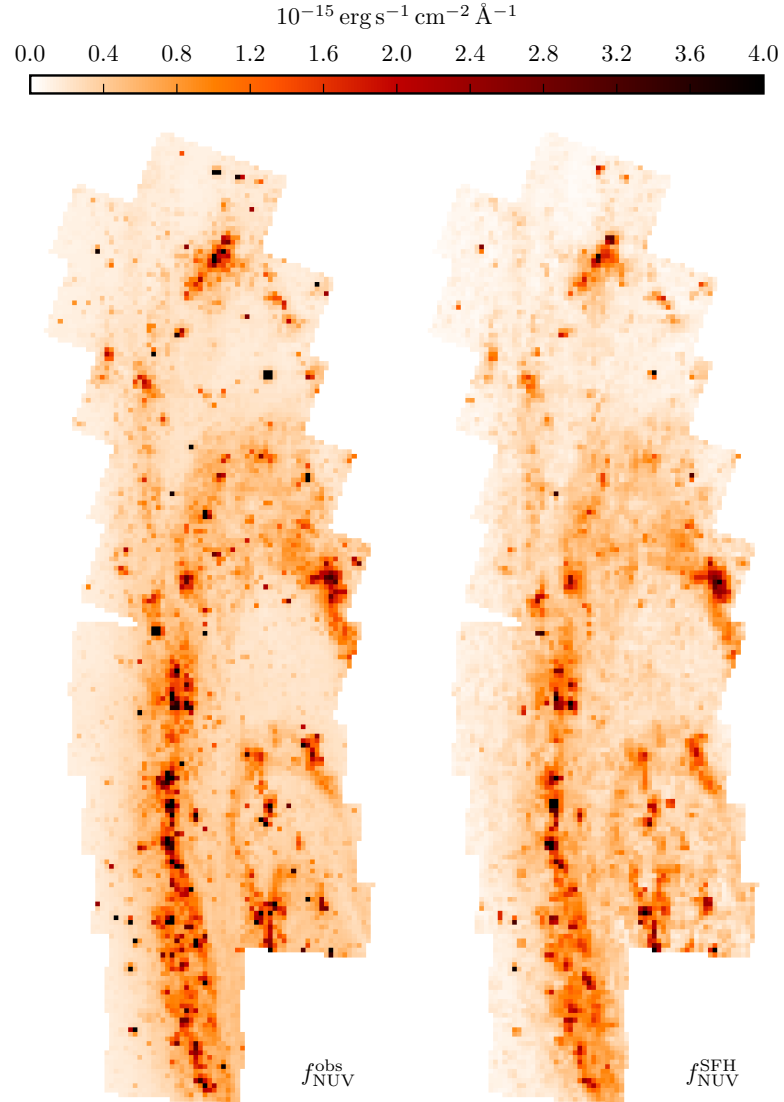


Figure 5. Same as Figure 4, but for the NUV filter.

slightly underestimated and overestimated, respectively, causing a significant downturn/upturn in the distribution of the $f_X^{\text{SFH}}/f_X^{\text{obs}}$ ratios for pixels with f_X^{obs} comparable to the background. To correct for this, we adjusted the background levels such that the median $\log_{10}(f_X^{\text{SFH}}/f_X^{\text{obs}})$ value for all pixels with $f_X^{\text{obs}} < 10^{-15.5} \text{ erg s}^{-1} \text{ cm}^{-2} \text{ Å}^{-1}$ (the approximate median of f_X^{obs}) matched that for all of the brighter pixels. The adjusted background values were 5.22×10^{-19} and $3.47 \times 10^{-19} \text{ erg s}^{-1} \text{ cm}^{-2} \text{ Å}^{-1} \text{ arcsec}^{-2}$ (2.9×10^{-16} and $2.0 \times 10^{-16} \text{ erg s}^{-1} \text{ cm}^{-2} \text{ Å}^{-1}$ per mosaic pixel) in FUV and NUV, respectively. We subtracted these values from the FUV and NUV mosaics to obtain the final observed UV flux maps for the PHAT survey area, f_X^{obs} , shown in Figures 4 (FUV) and 5 (NUV).

We emphasize that pixels with values comparable to the background ($f_X^{\text{obs}} \sim 10^{-15.5} \text{ erg s}^{-1} \text{ cm}^{-2} \text{ Å}^{-1}$) or fainter in Figures 4 and 5 are highly sensitive to the background subtraction method. This effect is partic-

ularly important for the distribution of the $f_X^{\text{SFH}}/f_X^{\text{obs}}$ ratios among the faint areas in the UV maps (§5.1). For the brighter pixels, the background subtraction method makes little difference.

4. SFR ESTIMATES

A common method for estimating the SFR of a target is to measure the integrated flux in one or more filters and then calculate the SFR using one of the flux-to-SFR calibrations available in the literature, e.g., (for UV flux) those discussed by Kennicutt (1998), Salim et al. (2007), Hao et al. (2011), Murphy et al. (2011), and Leroy et al. (2012); see also the review by Kennicutt & Evans (2012). We used this method to derive SFR maps for the PHAT survey area, which we later compared with similar maps derived from the SFHs (§2.1), extending the work of Simones et al. (2014) to a much larger sample that is more diverse in terms of UV brightness and star formation ac-

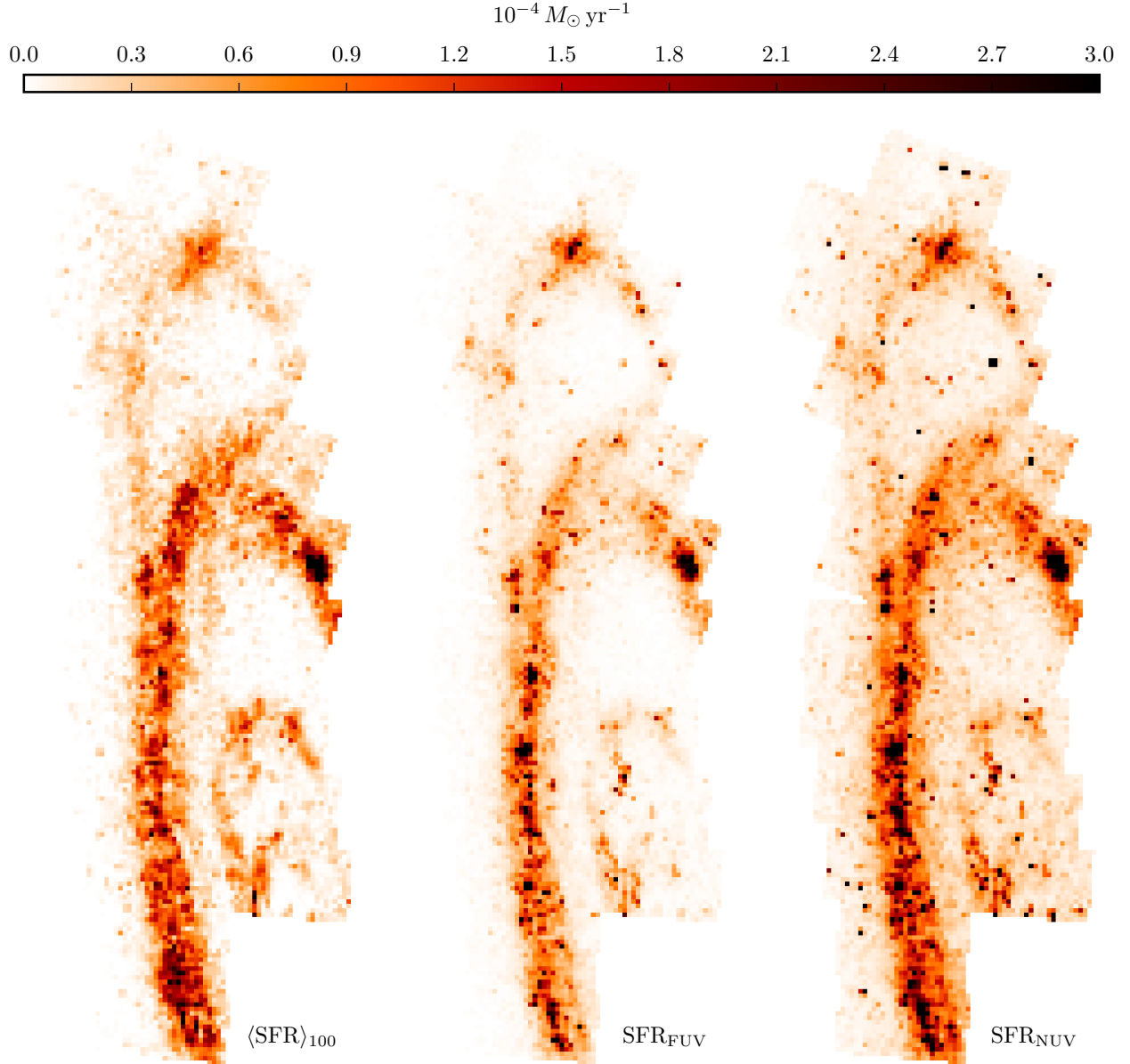


Figure 6. FUV and NUV flux-based SFRs, SFR_{FUV} (middle) and SFR_{NUV} (right), compared with $\langle \text{SFR} \rangle_{100}$ (left), the mean SFR over the last 100 Myr of the SFHs. The flux-based SFRs were derived from the observed GALEX fluxes, $f_{\text{FUV}}^{\text{obs}}$ and $f_{\text{NUV}}^{\text{obs}}$ (Figures 4 and 5), corrected for extinction using $A_{\text{FUV}}^{\text{SFH}}$ and $A_{\text{NUV}}^{\text{SFH}}$ (Figures 2 and 3). The SFR maps show good overall agreement.

tivity.

To calculate flux-based SFRs, we converted the f_X^{obs} maps into AB magnitudes, m_X^{obs} , (Equation 1) which we corrected for extinction by subtracting the synthetic A_X^{SFH} maps (§2.2). The extinction-corrected maps were converted back into (specific) fluxes ($\text{erg s}^{-1} \text{ cm}^{-2} \text{ \AA}^{-1}$), then into total fluxes ($\text{erg s}^{-1} \text{ cm}^{-2}$) by multiplying by the effective filter wavelengths in Table 1. The total fluxes were converted into luminosities, L_X (erg s^{-1}), assuming a distance modulus of 24.47 (McConnachie et al. 2005). Finally, we applied the calibrations from Kennicutt (1998) with updates by Hao et al. (2011) and Murphy et al. (2011) (see the review by Kennicutt & Evans

2012) to obtain the FUV and NUV flux-based SFR estimates, SFR_X , respectively:

$$\left(\frac{\text{SFR}_{\text{FUV}}}{M_\odot \text{ yr}^{-1}} \right) = 10^{-43.35} \left(\frac{L_{\text{FUV}}}{\text{erg s}^{-1}} \right) \quad (3)$$

$$\left(\frac{\text{SFR}_{\text{NUV}}}{M_\odot \text{ yr}^{-1}} \right) = 10^{-43.17} \left(\frac{L_{\text{NUV}}}{\text{erg s}^{-1}} \right) \quad (4)$$

These calibrations are based on stellar population synthesis using Starburst99 (Leitherer et al. 1999) and assume a constant SFR over the last 100 Myr, the Kroupa (2001) IMF, a fully populated range of masses from 0.1 to $100 M_\odot$, and solar metallicity (Hao et al. 2011).

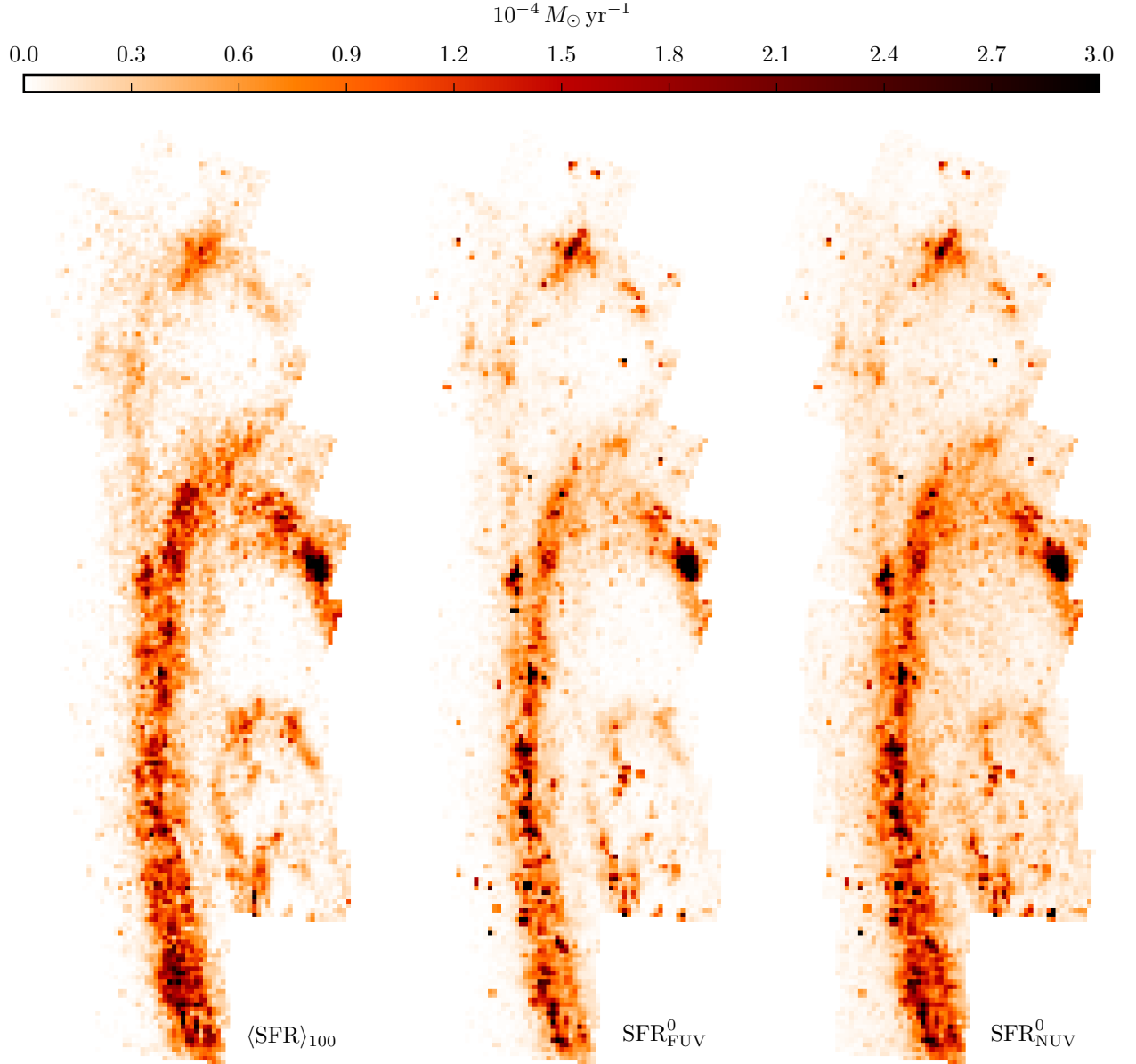


Figure 7. Same as Figure 6, but instead comparing $\langle \text{SFR} \rangle_{100}$ with $\text{SFR}_{\text{FUV}}^0$ and $\text{SFR}_{\text{NUV}}^0$, the SFRs from the synthetic intrinsic (i.e., unattenuated) fluxes from Figures 2 and 3. The synthetic intrinsic fluxes were derived assuming a fully populated IMF so there is no inconsistency with the flux calibration, which assumes the same. Like the SFRs based on observed flux, these SFRs also show good agreement with $\langle \text{SFR} \rangle_{100}$.

The most robust flux calibrations are those that rely on more than one part of the electromagnetic spectrum. An example of a hybrid estimator is the combination of *GALEX* FUV and *Spitzer* 24 μm fluxes, which simultaneously accounts for the direct starlight from newly formed massive stars and the absorbed starlight processed and reradiated by dust (e.g., Leroy et al. 2012). However, we have limited our study to observations by *GALEX*, so we will only consider the simpler monochromatic FUV and NUV calibrations in Equations 3 and 4. We show the final SFR_X maps in Figure 6.

To help determine the importance of SFH variability

on the SFRs calculated from Equations 3 and 4 (see §5.2), we created another pair of flux-based SFR maps derived as before, except we started with the intrinsic synthetic fluxes $f_X^{\text{SFH},0}$ described in §2.2. Because the fluxes were intrinsic, it was not necessary to apply an extinction correction before converting the fluxes into SFRs. The maps for the intrinsic flux-based SFR estimates, SFR_X^0 , are shown in Figure 7.

We also created a map for the mean SFR over the past 100 Myr of the SFHs, $\langle \text{SFR} \rangle_{100}$, which we show alongside the flux-based SFR maps in Figure 6. The 100 Myr limit represents the nominal timescale of UV emission

Table 3
Results.

Figure	Quantity	μ^a	σ^a	Median ^b	68% C.L. ^c	Unc. ^d
8	$f_{\text{FUV}}^{\text{SFH}}/f_{\text{FUV}}^{\text{obs}}$	7.62×10^{-3}	2.37×10^{-1}	1.02	0.59, 1.76	-0.43, +0.74
9	$f_{\text{NUV}}^{\text{SFH}}/f_{\text{NUV}}^{\text{obs}}$	-1.03×10^{-1}	1.59×10^{-1}	0.79	0.55, 1.14	-0.24, +0.35
*10	$\text{SFR}_{\text{FUV}}/\langle \text{SFR} \rangle_{100}$	-2.46×10^{-1}	2.61×10^{-1}	0.57	0.31, 1.04	-0.26, +0.47
*11	$\text{SFR}_{\text{NUV}}/\langle \text{SFR} \rangle_{100}$	9.27×10^{-2}	2.33×10^{-1}	1.24	0.72, 2.12	-0.52, +0.88
*12	$\text{SFR}_{\text{FUV}}^0/\langle \text{SFR} \rangle_{100}$	-1.98×10^{-1}	2.39×10^{-1}	0.63	0.37, 1.10	-0.27, +0.47
*13	$\text{SFR}_{\text{NUV}}^0/\langle \text{SFR} \rangle_{100}$	9.43×10^{-3}	2.08×10^{-1}	1.02	0.63, 1.65	-0.39, +0.63

^a μ and σ represent the location and scale parameters of the quantity's log-normal distribution.

^b Calculated from the location parameter as 10^μ .

^c Lower and upper 68% confidence limits, $10^{\mu \pm \sigma}$.

^d Lower and upper uncertainties as the difference between the median and the 68% confidence limits.

* Statistics apply only to pixels with $\langle \text{SFR} \rangle_{100} \geq 10^{-5} M_\odot \text{ yr}^{-1}$.

and matches the timescale used by Hao et al. (2011) to derive the FUV and the NUV flux calibrations.

5. DISCUSSION

5.1. Modeled flux

Figures 4 and 5 show remarkable overall qualitative agreement between the synthetic attenuated fluxes f_X^{SFH} (derived from optical CMDs) and the observed *GALEx* fluxes f_X^{obs} . In particular, all of the main features brighter than $\sim 10^{-15} \text{ erg s}^{-1} \text{ cm}^{-2} \text{ \AA}^{-1}$ in the observed maps are reproduced in the synthetic maps. This includes the main rings at $\sim 5, 10$, and 15 kpc from the center of M31, and the large star-forming complexes found in PHAT bricks 15 and 21. However, in detail we find distinct differences between the f_X^{SFH} and f_X^{obs} . Possible sources for these differences are discussed below.

The f_X^{obs} maps show several point sources which are not present in the f_X^{SFH} maps. These are most likely foreground stars that are lost in the synthetic maps because the fluxes were not derived for individual stars, but from SFHs that correspond to the *distributions* of stars in the CMDs. Likewise, there are some apparent point sources in the f_X^{SFH} maps that are not in the f_X^{obs} maps. We attribute these to photometric artifacts (e.g., diffraction spikes) remaining in the PHAT photometry despite applied quality puts (Dalcanton et al. 2012). The presence of photometric artifacts in a region increases the stellar mass measured in the region's SFH, thereby increasing the synthetic flux. Although foreground stars and photometric artifacts ruin the comparison between f_X^{SFH} and f_X^{obs} , such contamination only affects a small minority of the pixels in the maps.

We compare the synthetic and observed fluxes more quantitatively in Figures 8 (FUV) and 9 (NUV), which map the ratio of f_X^{SFH} to f_X^{obs} over the PHAT survey area. The Figures also show the flux ratios as a function of f_X^{obs} . We find that the log flux ratios follow normal distributions with mean $\mu = 7.62 \times 10^{-3}$ and standard deviation $\sigma = 2.37 \times 10^{-1}$ for FUV, and $\mu = -1.03 \times 10^{-1}$ and $\sigma = 1.59 \times 10^{-1}$ for NUV. In linear terms, the median flux ratios are 1.02 in FUV and 0.79 in NUV, with 68% confidence limits of 0.59 and 1.76 (FUV) and 0.55 and 1.14 (NUV). These results are summarized in Table 3. Note that in both filters, the median ratio is within the confidence interval of 1, indicating that f_X^{SFH} is overall consistent with f_X^{obs} .

The overall agreement between f_X^{SFH} and f_X^{obs} shows

that our modeling procedure is generally robust and justifies the several key assumptions used to derive f_X^{SFH} from the optical CMDs. Specifically, we assumed an IMF, models describing stellar spectra and evolution, and an extinction model as well as an extinction curve. These form the foundation for much research in astronomy and encompass our current best understanding of stellar astrophysics and star formation. It is therefore reassuring that we can use all of this knowledge to derive SFHs, synthesize SEDs, and successfully recreate detailed maps of a galaxy, all from photometry in just two optical bands.

The Poisson uncertainties in f_X^{obs} are relatively small. Assuming an average exposure time of 7×10^3 s in the FUV channel for the five DIS images in our study, the uncertainties are only a few percent at $f_{\text{FUV}}^{\text{obs}} \sim 10^{-16} \text{ erg s}^{-1} \text{ cm}^{-2} \text{ \AA}^{-1}$ and a few tenths of a percent at $f_{\text{FUV}}^{\text{obs}} \sim 10^{-14} \text{ erg s}^{-1} \text{ cm}^{-2} \text{ \AA}^{-1}$. The corresponding NUV uncertainties for an average exposure time of 6×10^4 s in the NUV channel are about one tenth of those in the FUV. However, Figures 8 and 9 show variances that are much larger than the Poisson uncertainties allow. These variances are therefore due almost exclusively to systematic effects in the modeling process, which we discuss below.

The primary systematic effect at play is most likely incomplete sampling of the IMF (Elmegreen 1999; Bastian et al. 2010; Fumagalli et al. 2011; da Silva et al. 2012, 2014). This explanation is supported by the observation that the variance in the flux ratios increases with decreasing pixel brightness, especially in the FUV filter. Also, the f_X^{SFH} maps show somewhat more uneven, noisy backgrounds, i.e., faint pixels in the off-arm areas of M31, compared with the f_X^{obs} maps. The faint pixels are associated with low star formation (SF) activity and, because all pixels are the same size, have fewer stars than the brighter pixels covering the arms and main star-forming regions. This leads to a violation of the full-IMF assumption used by FSFS and other stellar population synthesis codes.

Any sample of a given total stellar mass can have a higher (or lower) proportion of high-mass stars than expected for a fully populated IMF. There will therefore be more (or less) high-energy photons than stellar population synthesis models suggest, and the synthetic UV flux will be underestimated (or overestimated). In other words, when a stellar population is small, the same total

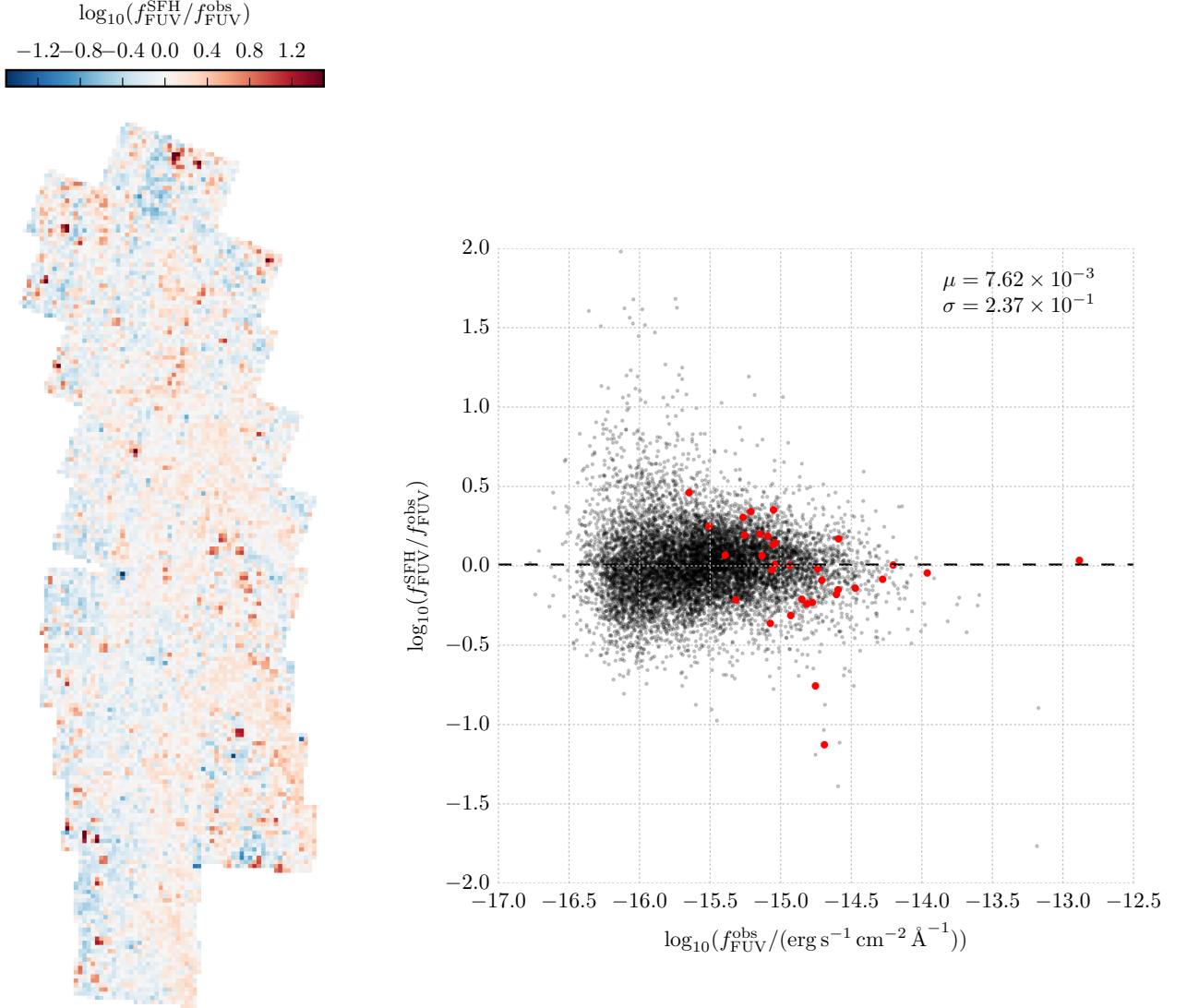


Figure 8. Ratio of the synthetic attenuated flux, $f_{\text{FUV}}^{\text{SFH}}$, to the GALEX observed flux, $f_{\text{FUV}}^{\text{obs}}$, in the FUV filter. The log flux ratios in the scatter plot follow a normal distribution with $\mu = 7.62 \times 10^{-3}$ (horizontal dashed line) and $\sigma = 2.37 \times 10^{-1}$. The median ratio is 1.02 with 68% confidence limits of 0.59 and 1.76. $f_{\text{FUV}}^{\text{SFH}}$ and $f_{\text{FUV}}^{\text{obs}}$ are therefore consistent on average. The flux ratio variance increases with decreasing observed flux, suggesting that the uncertainties are dominated by incomplete IMF sampling. The large red circles represent flux ratios for the UV-bright regions from Simones et al. (2014) and are consistent with the main sample. The map shows a fairly even spatial distribution for the flux ratios, with the most severely overestimated and underestimated pixels occurring primarily in the faint, off-arm areas of the galaxy, as shown in the scatter plot.

mass could be produced by a variety of mass functions (samplings of the IMF), where each mass function has its own unique luminosity. This sampling effect results in a variance in the flux ratios that increases with decreasing surface brightness. We observe that this trend is more pronounced in FUV, as mentioned above, due to the increased sensitivity of $f_{\text{FUV}}^{\text{obs}}$ to slight variations in the number of high-mass stars relative to $f_{\text{NUV}}^{\text{obs}}$.

Although IMF sampling more severely affects the fainter pixels, the sub-kpc resolution of our flux maps results in small pixel areas such that IMF sampling is likely the dominant source of the variance for all of the flux ratios. Accounting for projection effects in the disk, the physical area of each pixel is $4.4 \times 10^4 \text{ pc}^2$ (§2.2).

This is approximately equal to the average area of the UV-bright regions considered by Simones et al. (2014), who showed that the uncertainties in fluxes modeled for UV-bright regions decreases with increasing area. They also showed that combining several small regions into a larger \sim kpc-sized region greatly improved the agreement between the synthetic and observed fluxes. Taken together, these results show that the best way to comply with the full-IMF assumption and reduce the uncertainties in $f_{\text{X}}^{\text{SFH}}$ is to make the mosaic pixel size larger, thereby increasing the number of stars sampled. Naturally, reducing uncertainties this way comes at the cost of decreased spatial resolution in the flux maps. Exploring simultaneously the effects of both surface brightness and

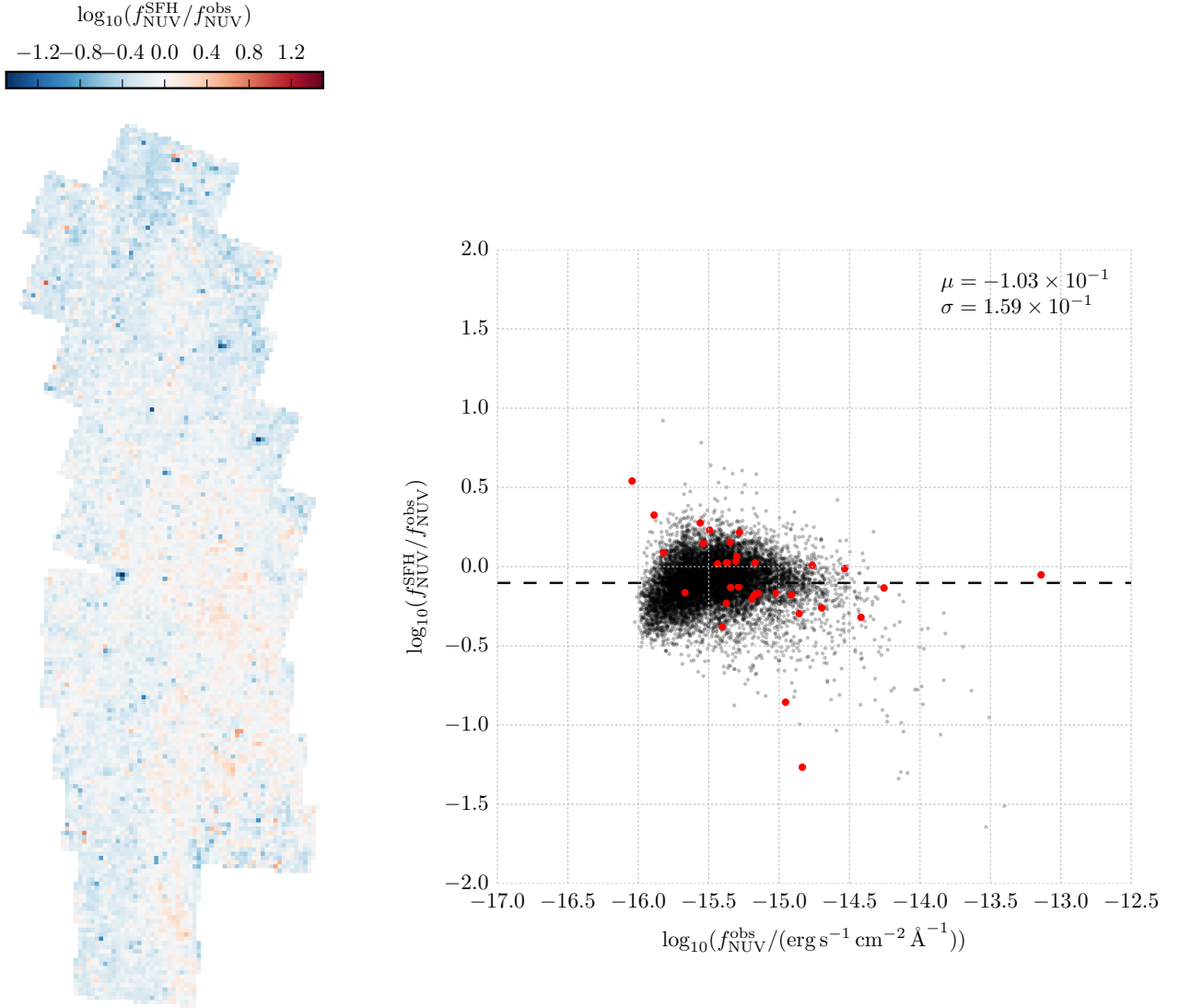


Figure 9. Same as Figure 8, but for the NUV filter. In this case, the log-normal distribution is characterized by $\mu = -1.03 \times 10^{-1}$ and $\sigma = 1.59 \times 10^{-1}$. The median ratio is 0.79 with 68% confidence limits of 0.55 and 1.14. $f_{\text{NUV}}^{\text{SFH}}$ and $f_{\text{NUV}}^{\text{obs}}$ are therefore consistent on average. The role of IMF sampling is not as important for $f_{\text{NUV}}^{\text{obs}}$, so the uncertainties in $f_{\text{NUV}}^{\text{obs}}$ are somewhat smaller.

pixel area on this fundamental, stochastic variance is a topic for future study.

As discussed previously, a small subset of our data are contaminated by foreground stars and photometric artifacts. We find that these sources of contamination drive many of the highest and lowest ratios in Figures 8 and 9. Milky Way foreground stars can emit ultraviolet fluxes comparable to the massive main sequence stars in M31. Excluding such stars from the CMDs, due to, e.g., photometric quality cuts or the CMD exclusion area, results in SFHs that (correctly) represent the stars that actually belong to M31. This mismatch causes the observed flux to be significantly higher than the synthetic flux, and thus leads to very low flux ratios. While many of the highest flux ratios are consistent with discrete IMF sampling in low-flux regions, some of the high ratios are explained by the misidentification of photometric artifacts

as massive stars in the CMDs. These lingering artifacts contribute false mass to resulting SFHs and increase the synthetic fluxes, dramatically increasing the flux ratios for the faintest regions.

We have added the flux ratios for the sample of UV-bright regions in Simones et al. (2014) to Figures 8 and 9 (red circles). Although the UV-bright regions vary in size and come from one small part of M31, their flux ratios appear to agree with the overall distribution for the rest of the galaxy. Also, other than the increased variance in the faint areas, we find no obvious trends in the mean or variance of the flux ratios with respect to environment or distance from the bulge. Therefore, we conclude that the flux modeling procedure may be successfully applied to any population in environments similar to M31. From the 68% confidence limits in the flux ratio distributions, we estimate the uncertainties in synthesizing fluxes for

sub-kpc regions to be $+0.74/-0.43$ and $+0.35/-0.24$ times the observed flux in FUV and NUV, respectively (Table 3). These uncertainties are driven mostly by incomplete sampling of the IMF and are consistent with Simones et al. (2014), who found uncertainties of $+0.95/-0.47$ for the synthetic FUV fluxes of the UV-bright regions.

5.2. SFR estimates from UV flux

As with the synthetic and observed fluxes, the flux-based SFR maps in Figures 6 and 7 show good overall morphological agreement with the CMD-based $\langle \text{SFR} \rangle_{100}$ map. We compare the SFRs more closely in Figures 10 and 11, where we map the ratio of SFR_X to $\langle \text{SFR} \rangle_{100}$ and plot the SFR ratio as a function of $\langle \text{SFR} \rangle_{100}$. A major feature in both figures is the marked contrast in the ratios between the high SFR areas and the low SFR areas. The areas with low $\langle \text{SFR} \rangle_{100}$, corresponding to the faint areas in Figures 4 and 5, host nearly all of the very highest SFR ratios in the entire survey area and none of the low or moderate ratios. The pixels in these areas make up the downward sloping tails seen at low $\langle \text{SFR} \rangle_{100}$ in the scatter plots in Figures 10 and 11.

The low-SFR tails are distinctly linear, with slopes of -1 and intercepts of -6.0 and -5.4 for the FUV and NUV SFR ratios, respectively. In log space, a straight line with -1 slope indicates that SFR_X becomes constant with a value equal to $10^{-6.0} = 9.8 \times 10^{-7} M_\odot \text{ yr}^{-1}$ for FUV and $10^{-5.4} = 4.1 \times 10^{-6} M_\odot \text{ yr}^{-1}$ for NUV. Because SFR_X is directly proportional to f_X^{obs} , these SFR constants suggest that there must be a constant baseline flux present in the galaxy that becomes more apparent as $\langle \text{SFR} \rangle_{100}$ decreases to very small values. Thus, the linear relationship between flux and SFR assumed by the flux calibrations in Equations 3 and 4 appear to break down completely below $\langle \text{SFR} \rangle_{100}$ approximately one to a few $\times 10^{-6} M_\odot \text{ yr}^{-1}$.

Using the flux calibrations in reverse, we find that the above SFR constants translate into $f_{\text{FUV}}^{\text{obs}} \sim 2 \times 10^{-16} \text{ erg s}^{-1} \text{ cm}^{-2} \text{ \AA}^{-1}$ and $f_{\text{NUV}}^{\text{obs}} \sim 8 \times 10^{-16} \text{ erg s}^{-1} \text{ cm}^{-2} \text{ \AA}^{-1}$ (or -15.7 and -15.1 in log flux, respectively). Figures 6, 7, 8, and 9 show that these flux and SFR limits make the FUV and NUV flux-to-SFR calibrations unreliable for approximately half of the pixels in the survey area. This demonstrates the importance of warnings in the literature (e.g., Murphy et al. 2011; Kennicutt & Evans 2012; Leroy et al. 2012) that flux calibrations are problematic on sub-kpc scales. We therefore limit our analysis of the SFR ratios in Figures 10 and 11 to pixels with $\langle \text{SFR} \rangle_{100}$ greater than a conservative threshold of $10^{-5} M_\odot \text{ yr}^{-1}$.

Considering only pixels with $\langle \text{SFR} \rangle_{100} \geq 10^{-5} M_\odot \text{ yr}^{-1}$, we treat the SFR ratios as having log-normal distributions with $\mu = -2.46 \times 10^{-1}$ and $\sigma = 2.61 \times 10^{-1}$ for FUV, and $\mu = 9.27 \times 10^{-2}$ and $\sigma = 2.33 \times 10^{-1}$ for NUV (Table 3). The median ratios are 0.57 (FUV) and 1.24 (NUV), with 68% confidence limits of 0.31 and 1.04 (FUV) and 0.72 and 2.12 (NUV), indicating that SFR_X is consistent with $\langle \text{SFR} \rangle_{100}$ overall. However, given the small uncertainties for the observed fluxes (§2.2) the large variances of the SFR ratios suggest that significant systematic effects are involved in the flux-to-SFR conversion process. We discuss these effects, including metallicity and IMF sampling, below.

One of the assumptions made by the flux calibrations in Equations 3 and 4 is that the input flux is produced by a stellar population with solar metallicity. The mean metallicity of the brick grid regions (§2.2) is $[\text{M}/\text{H}] = -0.06$ with a standard deviation of 0.09, so the mosaic pixels are consistent with solar metallicity on average. From Simones et al. (2014), overestimating $[\text{M}/\text{H}]$ by 0.1 dex causes the SFR to be overestimated by 0.015 dex. Therefore, the variation in the metallicities contributes only 0.01 dex to the variation in the log SFR ratios, making metallicity unimportant for the overall SFR ratio distribution.

Like the modeled fluxes in §5.1, the flux calibrations also assume a fully populated IMF, causing SFR_X to be overestimated (or underestimated) for pixels with an apparent excess (or lack) of massive stars. Also, if incomplete IMF sampling is the primary source of the variance in the log SFR ratios, as it is for the log flux ratios, then the σ parameters of the log-normal distributions should be similar. Indeed, we find consistent variances between Figures 8 and 10 and between Figure 9 and 11.

The flux calibrations also assume a constant SFH over the last 100 Myr. The analysis of UV-bright regions in Simones et al. (2014) showed that inconsistencies with this assumption can contribute at least as much to the total uncertainty in SFR_{FUV} as incomplete IMF sampling. To isolate the effect of SFH variability, we recreate in Figures 12 and 13 the maps and plots of Figures 10 and 11 using SFR_X^0 , the SFRs derived from the synthetic intrinsic fluxes (see §2.2) instead of SFR_X .

SFR_X^0 is a useful quantity because it is determined self-consistently. Converting a SFR (e.g., for an age bin in a SFH) into a flux as demonstrated in §2.2 is conceptually the inverse of converting a flux into a SFR via Equations 3 and 4. Also, both the synthetic fluxes and the flux calibrations assume a well-sampled IMF from Kroupa (2001). The only effect that would cause a difference between $\langle \text{SFR} \rangle_{100}$ and SFR_X^0 for a given SFH is variability in the SFH itself. We find little difference between the SFR ratio distributions in Figures 10 and 12 and in Figures 11 and 13. If SFH variability does play a role in the SFR ratio variances, then we cannot detect it on a statistically significant basis and it is therefore not a major contributor to the SFR_X and SFR_X^0 uncertainties.

The FUV SFR ratios from Simones et al. (2014) are shown in Figures 10 and 12 and appear to follow the distributions for the main sample. Comparing the μ and σ values between the two samples, we find that the means are consistent. Part of the discussion in Simones et al. (2014) concerned possible explanations for the apparent overestimation of SFRs relative to $\langle \text{SFR} \rangle_{100}$. However, in the context of our larger, survey-wide sample we see that the SFR ratios of the UV-bright regions are consistent on average.

In Figures 10, 11, 12, and 13, we do not observe any environmental trends for the mean or variance of SFR_X and SFR_X^0 , with the exception of the faintest areas of the galaxy responsible for the tails in the log SFR ratios distributions. Deriving SFRs from published flux calibrations is therefore generally a safe practice for environments like M31, *but only as long as the resulting SFRs are greater than $\sim 10^{-5} M_\odot \text{ yr}^{-1}$* . When applied to sub-kpc regions, we estimate the resulting uncertainties to be $+0.47/-0.26$ (FUV) and $+0.88/-0.52$ (NUV) times

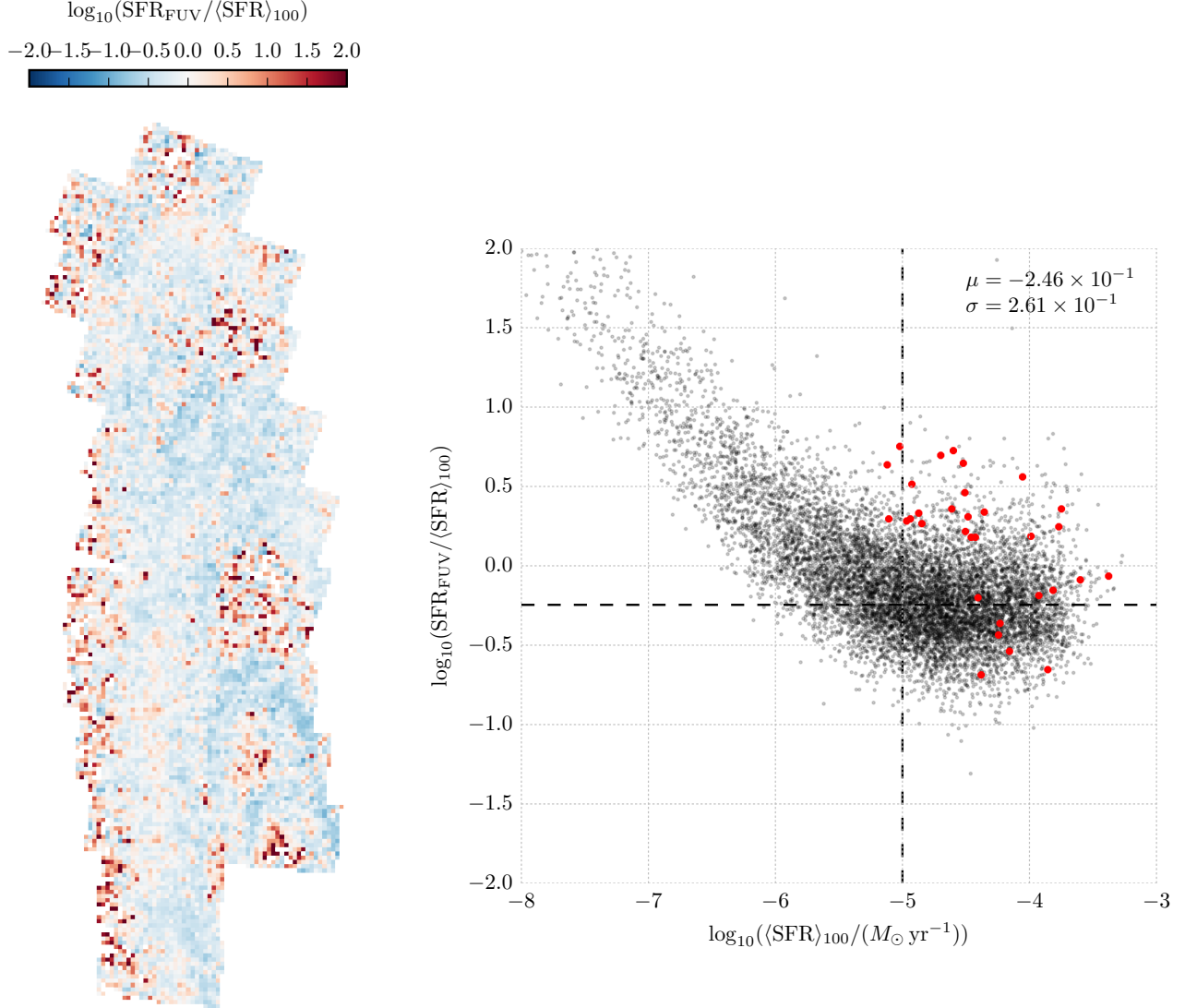


Figure 10. Ratio of the SFR based on the observed extinction-corrected FUV flux, SFR_{FUV} , to the 100 Myr mean of the SFH, $\langle \text{SFR} \rangle_{100}$. The log SFR ratios show a linear tail feature with -1 slope and -6.0 intercept, implying that SFR_{FUV} becomes constant for $\langle \text{SFR} \rangle_{100} < 9.8 \times 10^{-7} M_\odot \text{yr}^{-1}$. We constrain our analysis to pixels with $\langle \text{SFR} \rangle_{100} 10^{-5} M_\odot \text{yr}^{-1}$ (vertical dashed line). Above this limit, the log SFR ratios follow a normal distribution with $\mu = -2.46 \times 10^{-1}$ (horizontal dashed line) and $\sigma = 2.61 \times 10^{-1}$. The median ratio is 0.57 with 68% confidence limits of 0.31 and 1.04 , most likely due to incomplete IMF sampling. SFR_{FUV} and $\langle \text{SFR} \rangle_{100}$ are therefore consistent on average. The large red circles represent SFR ratios for the UV-bright regions from Simones et al. (2014) and are consistent with the main sample. Apart from the faint, off-arm areas responsible for the tail feature, the map shows a fairly even spatial distribution for the SFR ratios.

the true, underlying 100 Myr-mean SFR (Table 3). The SFR_{FUV} uncertainty is rather less than the $+2.15/-0.88$ uncertainty found by Simones et al. (2014).

Finally, we evaluate the flux calibrations in Equations 3 and 4 for \sim galaxy-sized scales, as they are perhaps more commonly used, by measuring the global SFR for the entire PHAT survey area. Summing all of the pixels in Figure 6, we find that $\langle \text{SFR} \rangle_{100} = 0.30 M_\odot \text{yr}^{-1}$, consistent with Lewis et al. (2015). In comparison, the global SFRs from the observed fluxes are $0.22 M_\odot \text{yr}^{-1}$ for FUV and $0.43 M_\odot \text{yr}^{-1}$ for NUV. If we adopt the estimated uncertainties mentioned earlier in this section, then the global flux-based SFRs are well within uncer-

tainty of $\langle \text{SFR} \rangle_{100}$. However, as larger areas are considered, IMF sampling effects should eventually disappear and the variances in the SFR ratios should correspondingly decrease. Therefore, our estimated uncertainties should be considered firm upper limits when applied to galaxies. The global SFR ratios (flux-based to mean) are 0.73 and 1.43 for FUV and NUV, respectively. Why these ratios are larger than the median ratios above is not yet understood.

6. CONCLUSION

We have used star formation histories (SFHs) to model the spectral energy distributions (SEDs) of over 9000 sub-kpc regions in M31 and produce detailed maps of

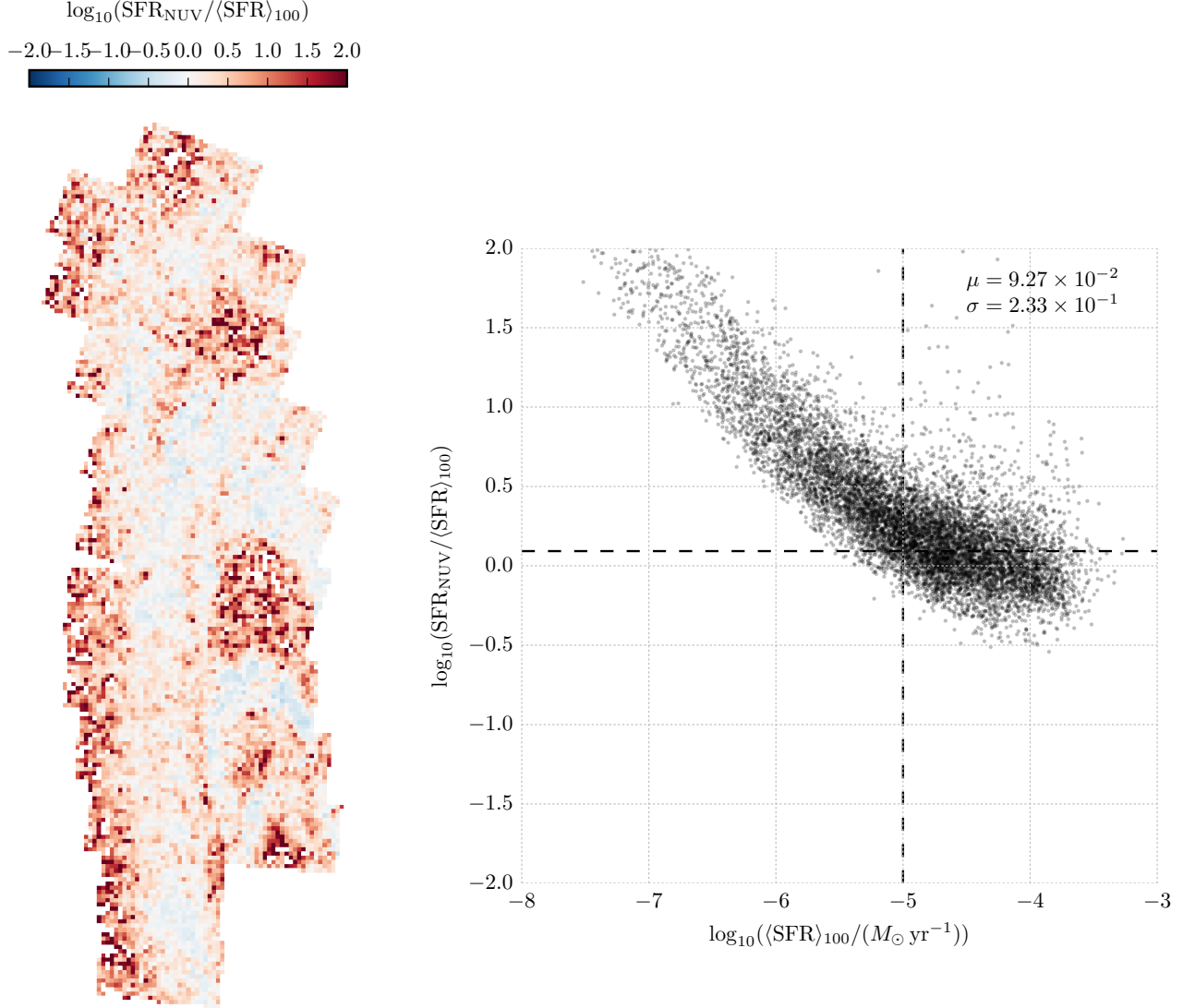


Figure 11. Same as Figure 10, but for the NUV filter. In this case, the linear tail has an intercept of -5.4 such that SFR_{NUV} becomes constant for $\langle \text{SFR} \rangle_{100} < 4.1 \times 10^{-6} M_{\odot} \text{ yr}^{-1}$. The log-normal distribution is characterized by $\mu = 9.27 \times 10^{-2}$ and $\sigma = 2.33 \times 10^{-1}$. The median ratio is 1.24 with 68% confidence limits of 0.72 and 2.12. SFR_{NUV} and $\langle \text{SFR} \rangle_{100}$ are therefore consistent on average.

synthetic UV flux across the entire area covered by the Panchromatic Hubble Andromeda Treasury (PHAT). This work is an extensive follow-up to the analysis of Simones et al. (2014), which involved only 33 ultraviolet (UV)-bright regions from a small portion of the galaxy. The SFHs were derived by Lewis et al. (2015) using F475W and F814W photometry from the PHAT survey. Both intrinsic and attenuated SEDs were derived from the SFHs using the Flexible Stellar Population Synthesis (FSPS) code. These were convolved with the Galaxy Evolution Explorer (*GALEX*) FUV and NUV response synthetic attenuated fluxes, f_X^{SFH} . All of the flux values were then assembled into an overall map, or mosaic, using Montage. The mosaic pixels corresponded to physical areas of $4.4 \times 10^4 \text{ pc}^2$. We constructed corresponding maps for the observed flux, f_X^{obs} , using *GALEX* Deep Imaging Survey (DIS) images.

The f_X^{SFH} maps agreed with the f_X^{obs} maps very well with respect to the broad morphology of M31, reproducing all of the main features brighter than $\sim 10^{-15} \text{ erg s}^{-1} \text{ cm}^{-2} \text{ \AA}^{-1}$. We found the log ratios of f_X^{SFH} to f_X^{obs} to be log-normally distributed with $\mu = 7.62 \times 10^{-3}$ and $\sigma = 2.37 \times 10^{-1}$ for FUV, and $\mu = -1.03 \times 10^{-1}$ and $\sigma = 1.59 \times 10^{-1}$ for NUV. The median flux ratios were 1.02 in FUV and 0.79 in NUV, with 68% confidence limits of 0.59 and 1.76 (FUV) and 0.55 and 1.14 (NUV). In both filters, the median ratio was within the confidence interval of 1, indicating that f_X^{SFH} was consistent with f_X^{obs} on average. Due to the small pixel areas, the primary source of the variance in the log flux ratios was most likely related to incomplete sampling of the IMF.

We found no obvious trends in the flux ratios with respect to environment, except for in the faintest, off-arm areas of M31 where the variances in the flux ra-

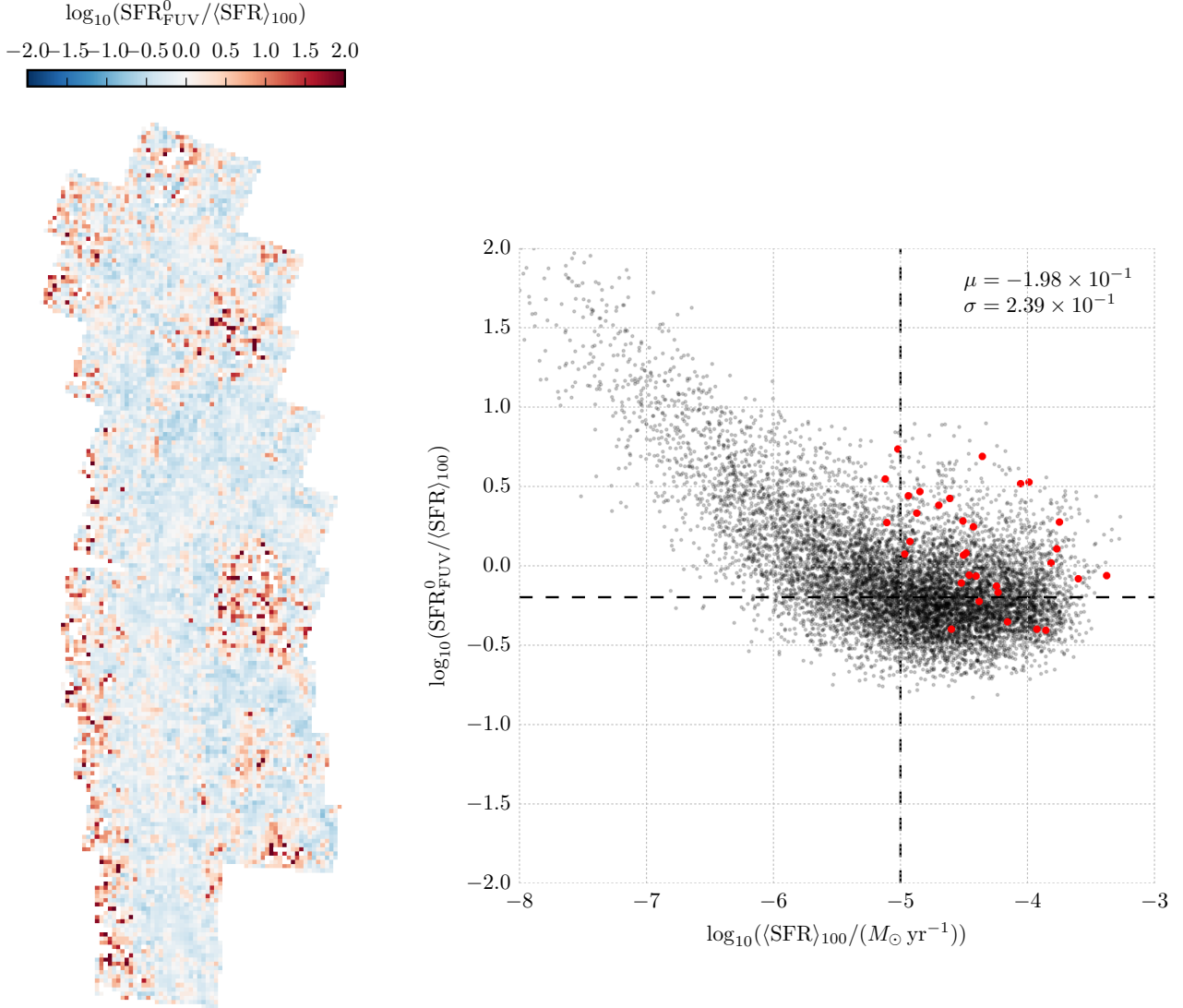


Figure 12. Same as Figure 10, but based on synthetic intrinsic flux, SFR_{FUV}^0 . The log-normal distribution is characterized by $\mu = -1.98 \times 10^{-1}$ and $\sigma = 2.39 \times 10^{-1}$. The median ratio is 0.63 with 68% confidence limits of 0.37 and 1.10. SFR_{FUV}^0 and $\langle SFR \rangle_{100}$ are therefore consistent on average. The results here are similar to Figure 10, suggesting that SFH variability does not significantly affect the SFR_{FUV} uncertainties.

tios were noticeably larger. We conclude that fluxes may be successfully modeled from SFHs for any population in environments similar to M31. For our sub-kpc regions, we estimate the synthetic flux uncertainties to be $+0.74/-0.43$ and $+0.35/-0.24$ in FUV and NUV, respectively. Results from previous work on UV-bright regions by Simones et al. (2014) were consistent with our results.

The overall agreement between the observed and synthetic fluxes is remarkable considering that our flux modeling procedure was dependent on several key assumptions. Specifically, we assumed an IMF, models describing stellar spectra and evolution, and an extinction model as well as an extinction curve. These form the foundation for much research in astronomy and encompass our current best understanding of stellar astrophysics and star formation. It is reassuring that we can use all of

this knowledge to successfully recreate detailed maps of a galaxy from photometry in just two optical bands.

We used flux calibrations from Kennicutt (1998) with updates by Hao et al. (2011) and Murphy et al. (2011) to estimate SFRs based on observed UV flux, SFR_X . The f_X^{obs} maps were first corrected for extinction using the synthetic attenuated and intrinsic fluxes. We also calculated the 100 Myr mean SFR from the SFHs, $\langle SFR \rangle_{100}$. We found that the faintest areas of M31 had the highest ratios of SFR_X to $\langle SFR \rangle_{100}$ and formed a linear tail feature in plots of the SFR ratio versus $\langle SFR \rangle_{100}$. These tails were the result of a distinct breakdown of the linear relationship between flux and SFR which underpins the flux calibration method. We estimated a conservative threshold of $SFR \sim 10^{-5} M_\odot \text{ yr}^{-1}$ below which flux calibration should not be used.

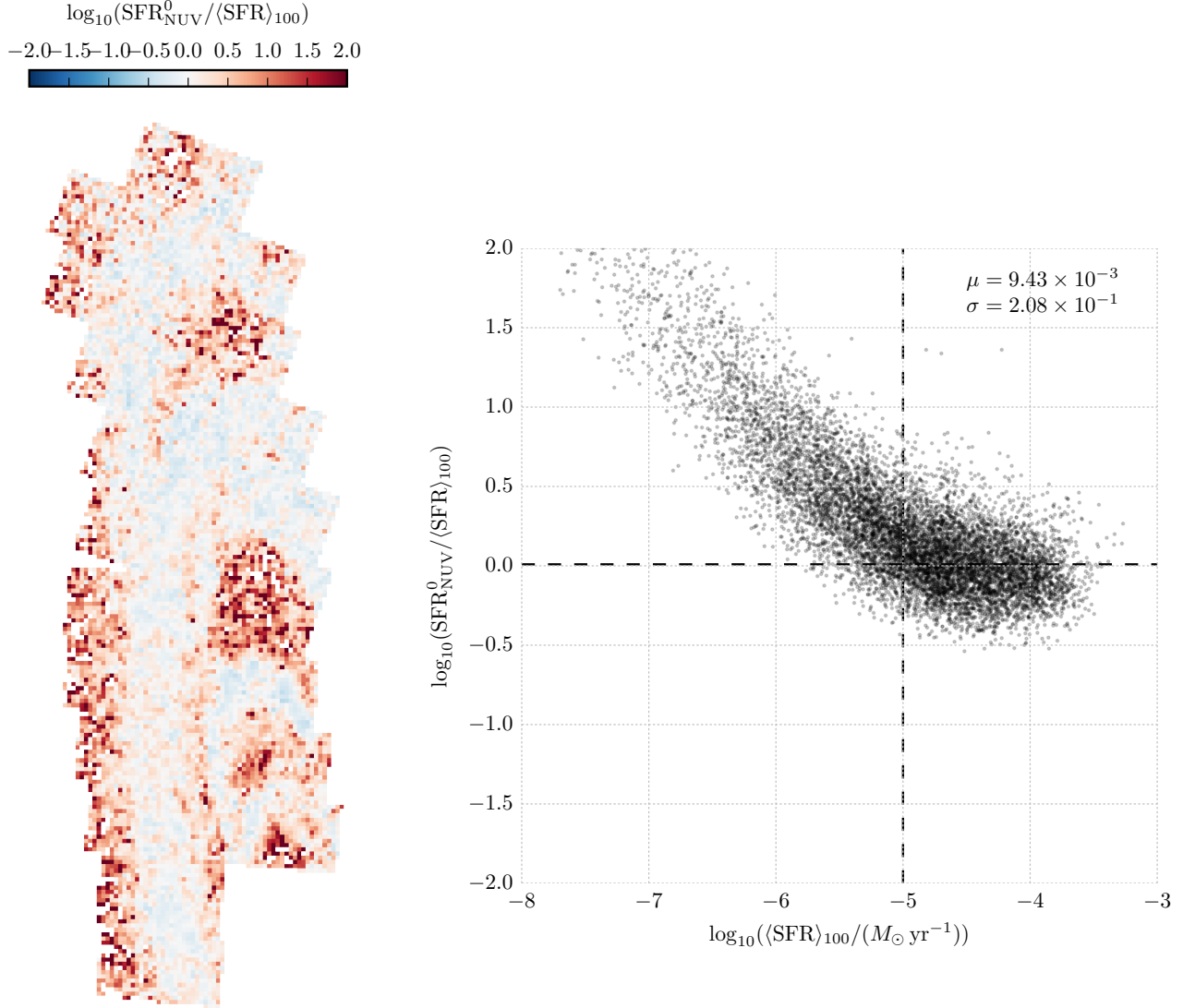


Figure 13. Same as Figure 11, but based on synthetic intrinsic flux, SFR_{NUV}^0 . The log-normal distribution is characterized by $\mu = 9.43 \times 10^{-3}$ and $\sigma = 2.08 \times 10^{-1}$. The median ratio is 1.02 with 68% confidence limits of 0.63 and 1.65. SFR_{NUV}^0 and $\langle SFR \rangle_{100}$ are therefore consistent on average. The results here are similar to Figure 11, suggesting that SFH variability does not significantly affect the SFR_{NUV} uncertainties.

For the pixels above this threshold, we found the SFR ratios to be log-normally distributed with $\mu = -2.46 \times 10^{-1}$ and $\sigma = 2.61 \times 10^{-1}$ for FUV, and $\mu = 9.27 \times 10^{-2}$ and $\sigma = 2.33 \times 10^{-1}$ for NUV. The median ratios are 0.57 (FUV) and 1.24 (NUV), with 68% confidence limits of 0.31 and 1.04 (FUV) and 0.72 and 2.12 (NUV), indicating that SFR_X is consistent with $\langle SFR \rangle_{100}$ on average. As with the flux ratios, incomplete sampling of the IMF was the main source of the variance in the SFR ratios. We also considered deviations from solar metallicity as well as SFH variability, and found that they were far less important for the overall variances in the SFR ratios than IMF sampling.

Other than the faintest, off-arm areas which are responsible for the tail feature in the SFR ratio distributions, there were no obvious trends in the SFR ratios

with respect to environment. We determine that the flux calibration method is safely applicable to environments similar to M31, *but only as long as the resulting SFRs are greater than $\sim 10^{-5} M_\odot \text{ yr}^{-1}$* . We estimate the SFR uncertainties for our sub-kpc regions to be $+0.47/-0.26$ (FUV) and $+0.88/-0.52$ (NUV) times the true, underlying 100 Myr-mean SFR. The SFR_{FUV} uncertainty is rather less than the $+2.15/-0.88$ uncertainty previously found by Simones et al. (2014).

We also measured global SFRs for the entire PHAT survey area. The global $\langle SFR \rangle_{100}$ value was $0.30 M_\odot \text{ yr}^{-1}$, while the UV flux-based values were $SFR_{FUV} = 0.22 M_\odot \text{ yr}^{-1}$ and $SFR_{NUV} = 0.43 M_\odot \text{ yr}^{-1}$. The flux-based global SFRs are consistent with the global $\langle SFR \rangle_{100}$ value to within the uncertainties derived from the SFR maps. However, the variances in the SFR ratios

due to IMF sampling is expected to decrease for larger areas, so our estimated uncertainties should be considered firm upper limits when applied to galaxies. The global SFR ratios (flux-based to mean) are 0.73 and 1.43 for FUV and NUV, respectively. Why these ratios are larger than the median ratios above is not yet understood.

This research has made use of NASA's Astrophysics Data System Bibliographic Services and the NASA/IPAC Extragalactic Database (NED), which is operated by the Jet Propulsion Laboratory, California Institute of Technology, under contract with the National Aeronautics and Space Administration. This work was supported by the Space Telescope Science Institute through GO-12055. Support for D. R. W is provided by NASA through Hubble Fellowship grant HST-HF-51331.01 awarded by the Space Telescope Science Institute, which is operated by the Association of Universities for Research in Astronomy, Inc., under NASA contract NAS 5-26555. This research made use of Astropy, a community-developed core Python package for Astronomy (Astropy Collaboration et al. 2013), as well as NumPy and SciPy (Oliphant 2007), IPython (Pérez & Granger 2007), and Matplotlib (Hunter 2007). This research made use of Montage, funded by the National Aeronautics and Space Administration's Earth Science Technology Office, Computation Technologies Project, under Cooperative Agreement Number NCC5-626 between NASA and the California Institute of Technology. Montage is maintained by the NASA/IPAC Infrared Science Archive.

REFERENCES

- Astropy Collaboration, Robitaille, T. P., Tollerud, E. J., et al. 2013, *A&A*, 558, A33
- Barmby, P., Huchra, J. P., Brodie, J. P., et al. 2000, *AJ*, 119, 727
- Bastian, N., Covey, K. R., & Meyer, M. R. 2010, *ARA&A*, 48, 339
- Bianchi, L., Clayton, G. C., Bohlin, R. C., Hutchings, J. B., & Massey, P. 1996, *ApJ*, 471, 203
- Calabretta, M. R., & Greisen, E. W. 2002, *A&A*, 395, 1077
- Cardelli, J. A., Clayton, G. C., & Mathis, J. S. 1989, *ApJ*, 345, 245
- Conroy, C., & Gunn, J. E. 2010, *ApJ*, 712, 833
- Conroy, C., Gunn, J. E., & White, M. 2009, *ApJ*, 699, 486
- da Silva, R. L., Fumagalli, M., & Krumholz, M. R. 2012, *ApJ*, 745, 145
- da Silva, R. L., Fumagalli, M., & Krumholz, M. R. 2014, *MNRAS*, 444, 3275
- Dalcanton, J. J., Williams, B. F., Lang, D., et al. 2012, *ApJS*, 200, 18
- de Vaucouleurs, G., de Vaucouleurs, A., Corwin, H. G., et al. 1995, *VizieR Online Data Catalog*, 7155, 0
- Dolphin, A. E. 2002, *MNRAS*, 332, 91
- Elmegreen, B. G. 1999, *ApJ*, 515, 323
- Fumagalli, M., da Silva, R. L., & Krumholz, M. R. 2011, *ApJ*, 741, L26
- Girardi, L., Williams, B. F., Gilbert, K. M., et al. 2010, *ApJ*, 724, 1030
- Gogarten, S. M., Dalcanton, J. J., Williams, B. F., et al. 2009, *ApJ*, 691, 115
- Gordon, K. D., Bailin, J., Engelbracht, C. W., et al. 2006, *ApJ*, 638, L87
- Hao, C.-N., Kennicutt, R. C., Johnson, B. D., et al. 2011, *ApJ*, 741, 124
- Hunter, J. D. 2007, *Computing in Science and Engineering*, 9, 90
- Johnson, B. D., Weisz, D. R., Dalcanton, J. J., et al. 2013, *ApJ*, 772, 8
- Kennicutt, R. C., & Evans, N. J. 2012, *ARA&A*, 50, 531
- Kennicutt, Jr., R. C. 1998, *ARA&A*, 36, 189
- Kroupa, P. 2001, *MNRAS*, 322, 231
- Leitherer, C., Schaerer, D., Goldader, J. D., et al. 1999, *ApJS*, 123, 3
- Leroy, A. K., Bigiel, F., de Blok, W. J. G., et al. 2012, *AJ*, 144, 3
- Lewis, A. R., Dalcanton, J. J., Dolphin, A. E., Weisz, D. R., & Williams, B. F. 2015, submitted
- Marigo, P., Girardi, L., Bressan, A., et al. 2008, *A&A*, 482, 883
- Martin, D. C., Fanson, J., Schiminovich, D., et al. 2005, *ApJ*, 619, L1
- Massey, P., Olsen, K. A. G., Hodge, P. W., et al. 2006, *AJ*, 131, 2478
- McConnachie, A. W., Irwin, M. J., Ferguson, A. M. N., et al. 2005, *MNRAS*, 356, 979
- McQuinn, K. B. W., Skillman, E. D., Dolphin, A. E., & Mitchell, N. P. 2015, submitted
- Morrissey, P., Conrow, T., Barlow, T. A., et al. 2007, *ApJS*, 173, 682
- Murphy, E. J., Condon, J. J., Schinnerer, E., et al. 2011, *ApJ*, 737, 67
- Oliphant, T. E. 2007, *Computing in Science and Engineering*, 9, 10
- Pérez, F., & Granger, B. E. 2007, *Computing in Science and Engineering*, 9, 21
- Salim, S., Rich, R. M., Charlot, S., et al. 2007, *ApJS*, 173, 267
- Simones, J. E., Weisz, D. R., Skillman, E. D., et al. 2014, *ApJ*, 788, 12
- Tully, R. B. 1994, *VizieR Online Data Catalog*, 7145, 0
- Westera, P., Lejeune, T., Buser, R., Cuisinier, F., & Bruzual, G. 2002, *A&A*, 381, 524
- Williams, B. F., Lang, D., Dalcanton, J. J., et al. 2014, *ApJS*, 215, 9